Electronic Supplementary Information for
Particle-Based and Continuum Models for Confined Nematics in Two Dimensions

H. Híjar and A. Majumdar

Abstract

This document includes: Appendices A to C; figures S1 to S4; legends for supplementary movies S1 to S12; and references. **Other supplementary files for this paper include**: Supplementary movies S1 to S12.

A Estimation of the nematic coherence length

The nematic coherence length and, consequently, λ can be estimated from measurements of $\mathscr{D}$ and K_{elas}/μ_1, as shown by equation (24). On the one hand, $\mathscr{D}$ can be related with single-particle rotational motion through the normalized time correlation functions [1]

$$\Phi^p_{mn}(t) = \frac{\left\langle D^{p*}_{mn}(\Omega(0))\, D^p_{mn}(\Omega(t))\right\rangle}{\left\langle D^{p*}_{mn}(\Omega(0))\, D^p_{mn}(\Omega(0))\right\rangle}, \tag{A1}$$

where $D^p_{mn}(\Omega(t))$ is the Wigner rotational matrix element of rank p and $\Omega = (\alpha_{\text{e}}, \beta_{\text{e}}, \gamma_{\text{e}})$ is a set of time-dependent Euler angles that specify particle's orientation with respect to the global director field, $\mathbf{n}_0$. It is customary to approximate $\Phi^p_{mn}(t)$ by a single exponential [1, 2]

$$\Phi^p_{mn}(t) = \Phi^p_{mn}(\infty) + [\Phi^p_{mn}(0) - \Phi^p_{mn}(\infty)] \exp\left(-\frac{t}{\tau_{mn}}\right), \tag{A2}$$

where the correlation time, τ_{mn}, is related with rotational diffusion constants of uniaxial particles through

$$\frac{1}{\tau_{mn}} = c_{mn}\mathscr{D} + n^2\left(\mathscr{D}' - \mathscr{D}\right). \tag{A3}$$

In equation (A3), n^2 is the square of the subscript in τ_{mn} and should not be confused with the square magnitude of the director field, $\mathscr{D}'$ describes spinning motion of a particle around its symmetry axis and c_{mn} are coefficients related with S and the fourth order scalar parameter, $S_4 = \langle 35(\mathbf{u}\cdot\mathbf{n})^4 - 30(\mathbf{u}\cdot\mathbf{n})^2 + 3\rangle/8$ [1]. With the aim of calculating $\mathscr{D}$ only, we focus our attention on second rank correlations ($p = 2$) with $m = n = 0$, for which $D^2_{00} = P_2(\cos\beta_{\text{e}})$. Here, P_2 is the second-rank Legendre polynomial and β_{e} reduces to the polar angle of individual orientations with respect to $\mathbf{n}_0$. The corresponding coefficient, c_{00}, is calculated in reference [3] and reads as

$$c_{00} = 6\frac{7 + 5S - 12S_4}{7 + 10S + 18S_4 - 35S^2}. \tag{A4}$$

We simulated 3D N-MPCD systems with volume $V = (56a)^3$, periodic boundary conditions to approximate macro-scale behavior, and $\mathbf{n}_0$ pointing along the x_3-axis of a Cartesian frame $\{x_1, x_2, x_3\}$. We

considered a density of 20 particles per collision cell, $\chi_{\mathsf{HI}} = 0$; and two collision times $\Delta t = 0.1$ and $1.0\,u_t$. The nematic phase is observed for $U \gtrsim 5$ [10]. Thus, we vary nematicities in the range from $U = 6$ to 12. We obtained $\Phi^2_{00}(t)$ from trajectories of orientations $\mathbf{u}^i$ fitting $\Phi^2_{00}(0)$, $\Phi^2_{00}(\infty)$, and τ_{00} in equation (A2) in the time interval from $2\Delta t$ to $20\Delta t$. Measurements of global order parameters S and S_4, and equations (A3) and (A4) yielded values of $\mathscr{D}$ reported in table 1.

Table 1: Estimations of the rotational diffusivity $\mathscr{D}$ (in units of u_t^{-1}), and the ratio K_{elas}/μ_1 (in units of $a\,u_t^{-1}$) as function of the N-MPCD nematicity U, and collision time-step Δt.

	$\Delta t = 0.1\,u_t$		$\Delta t = 1.0\,u_t$	
U	$\mathscr{D}$	K_{elas}/μ_1	$\mathscr{D}$	K_{elas}/μ_1
6	0.28	0.316	0.074	0.220
7	0.23	0.287	0.071	0.200
8	0.17	0.270	0.080	0.188
9	0.15	0.256	0.070	0.180
10	0.13	0.248	0.065	0.174
11	0.13	0.242	0.065	0.170
12	0.16	0.237	0.083	0.166

On the other hand, K_{elas}/μ_1 was obtained from dynamic spectra of local instantaneous director fluctuations defined as $\delta\mathbf{n}(\mathbf{r},t) = \mathbf{n}(\mathbf{r},t) - \mathbf{n}_0$. We used the set of simulations for calculating $\mathscr{D}$ to calculate also $K_{\mathsf{elas}}/\gamma_1$. Since in these simulations orientation and velocity fields are decoupled, N-MPCD fluids are contained in cubic volumes with periodic boundary conditions, and $\mathbf{n}_0$ points along the x_3-axis, we have [5]

$$\langle \delta\tilde{n}_\alpha(\mathbf{k},\omega)\,\delta\tilde{n}_\alpha(-\mathbf{k},-\omega)\rangle = \frac{A_n}{\omega^2 + (K_{\mathsf{elas}}/\gamma_1)^2 k^4}. \tag{A5}$$

where $\alpha = 1,2$ and no summation over repeated indices is implied. In equation (A5), we use a tilde to indicate Fourier transform from space and time coordinates, $\mathbf{r}$ and t, to wave vector and angular frequency coordinates, $\mathbf{k}$ and ω, respectively. Also in equation (A5), A_n can be considered a constant, γ_1 is a rotational viscosity related with μ_1 by $\gamma_1 = 2\mu_1/(9S^2)$; [4] and $\mathbf{k} = (k,0,0)$, with $k = 2\pi j V^{-1/3}$ and j a positive integer.

Following references [5, 6], we recorded time series of space Fourier transforms of $\delta\mathbf{n}$ according to

$$\delta\mathbf{n}(\mathbf{k},t) = \sum_{i=1}^{N} \left[\mathbf{u}^i(t) - \mathbf{n}_0\right] \exp\left(-\mathrm{i}\,\mathbf{k}\cdot\mathbf{r}^i(t)\right), \tag{A6}$$

where $\mathrm{i}^2 = -1$. These series permitted calculation of correlation functions which were subsequently Fourier transformed to the ω domain. The resulting curves were fitted by equation (A5) considering A_n and $K_{\mathsf{elas}}/\gamma_1$ as adjustable parameters. The latter showed a very small variation with respect to U, in agreement with previous measurements [5]. Then, we averaged the estimated ratio $K_{\mathsf{elas}}/\gamma_1$ over U, perpendicular fluctuations ($\alpha = 1,2$), and four different wave numbers ($j = 1,2,3,4$). Subsequently, calculations of S yielded the values of K_{elas}/μ_1 shown in table 1. We obtained ξ_{N} as function of U and Δt from measurements in table 1 and equation (24). Results, shown in figure 1, confirm that the radius of topological defects in N-MPCD is of the order of the collision cell size, i.e., $\xi_{\mathsf{N}} \lesssim a$ [7, 8]. Then, we fit data in figure 1 by cubic polynomials as in equation (25) yielding $a_0 = 2.11\,a$, $a_1 = -0.56\,a$, $a_2 = 0.065\,a$, and $a_3 = -0.003\,a$, for $\Delta t = 0.1\,u_t$; and $a_0 = 4.85\,a$, $a_1 = -1.28\,a$, $a_2 = 0.13\,a$, and $a_3 = -0.005\,a$, for $\Delta t = 1.0\,u_t$.

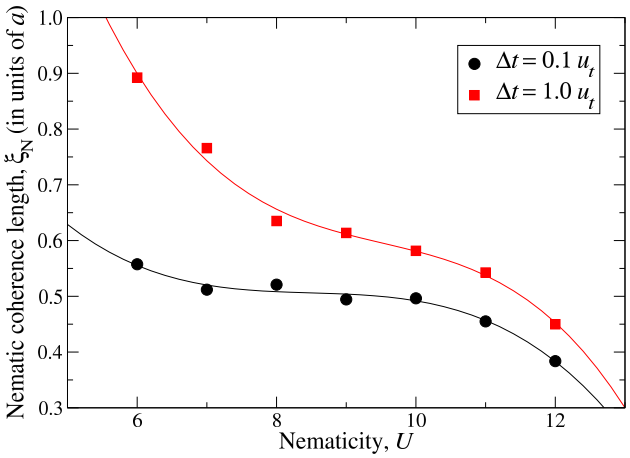

Figure S 1: Nematic coherence length in N-MPCD. Symbols are obtained from equation (24) and measurements of $\mathscr{D}$ and K/μ_1 (table 1). Curves represent regression models by cubic polynomials.

Under the same simulation conditions, L can be estimated from [9]

$$L = \frac{V k_{\mathrm{B}} T}{2k^2 \langle Q_{\alpha 3}(\mathbf{k})\, Q_{\alpha 3}(-\mathbf{k})\rangle}, \tag{A7}$$

where, again, $\alpha = 1,2$ and no summation is implied. We obtained the space Fourier transform of the order parameter tensor tensor from

$$Q_{\alpha 3}(\mathbf{k}) = \frac{3}{2N} \sum_{i=1}^{N} u_{\alpha}^{i}(t)\, u_{3}^{i}(t) \exp\left(-\mathrm{i}\mathbf{k}\cdot\mathbf{r}^{i}(t)\right), \tag{A8}$$

and measurements yielded $L = 176 k_B T/a$ for $U = 10$ and $\Delta t = 1\, u_t$, which is in the order of magnitude expected from previous calculations in N-MPCD [10, 11]. This value is used in equation (27) to get the numerical estimates of $F_{\mathsf{elas}}(t)$.

B Additional results for orientation patterns in squares

Figure S2 shows three instantaneous director patterns obtained after application of the orientation collision operator in simulations conducted at $U = 3$ and $R = 8a$. They are compared with the average field of figure 2 in the main text for the same U and R. It can be observed that fluctuations are stronger around regions of small S^{c}, as expected, whereas fluctuations are relatively small near the square edges.

Figure S3 shows WORS and *Diagonal* solutions obtained for nematicities $U = 3.0$, 3.2, and 3.4, maintaining $R = 8a$ and $\chi_{\mathsf{HI}} = 0$ to eliminate reorientation effects produced by spontaneous flow fluctuations. Also, we take Δt to be 0.1, 0.5, and $1\, u_t$, which correspond to different rates of application of multi-particle collision operator. WORS appears to be more stable at $\Delta t = 0.1\, u_t$. For this value, the WORS is observed up to $U = 3.4$, although a proto-diagonal structure is formed in the central region of the square. For larger Δt, the stability of the WORS is lost at smaller U.

C Solution to the equation of motion of $\mathbf{q}(t)$

To solve the system of equations (35) and (36), we write them in terms of polar coordinates q and θ. After substituting $q_1 = q\cos\theta$, and $q_2 = q\sin\theta$ into equations (35) and (36), and separating the

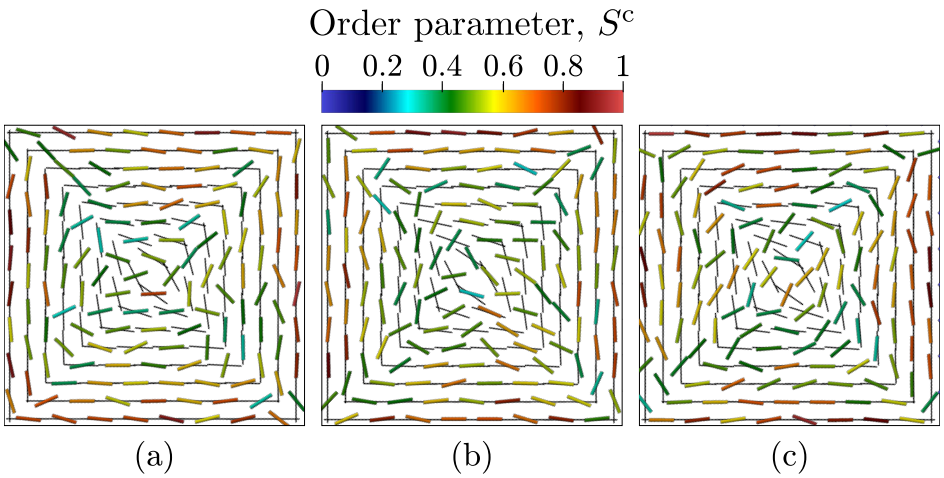

Figure S 2: Three snapshots of director configurations for a N-MPCD fluid within a square well ($U = 3$, $R = 8a$). Black lines indicate the average WORS whereas colored rods are instantaneous solutions after: (a) 1×10^3, (b) 2×10^3, and (c) 3×10^3 collisions steps from thermalization.

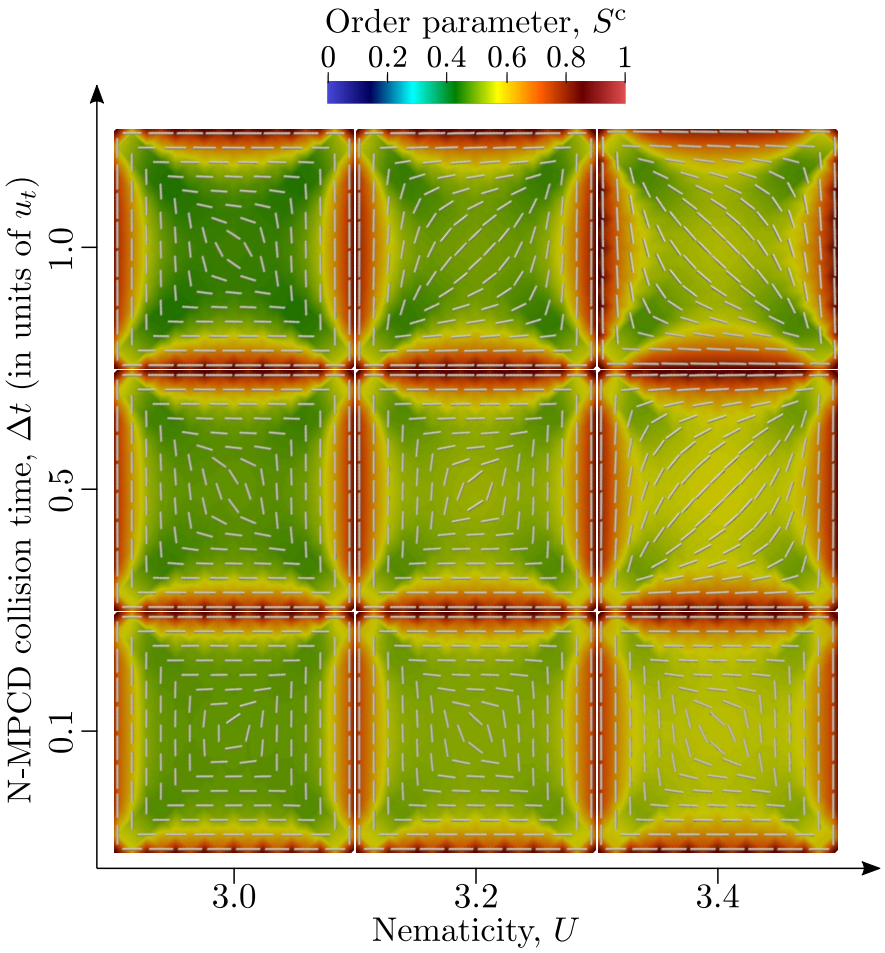

Figure S 3: Average textures for small squares ($R = 8a$) as function of U and Δt.

equations for dq/dt and $d\theta/dt$, we obtain

$$\frac{dq}{dt} = \zeta \left[\frac{1}{q} + \frac{q - l\cos\theta}{q^2 - 2ql\cos\theta + l^2} \right], \tag{C1}$$

$$\frac{d\theta}{dt} = \zeta \frac{l}{q} \frac{\sin\theta}{q^2 - 2ql\cos\theta + l^2}. \tag{C2}$$

We will solve equations (C1) and (C2) under a perturbation method where the motion of the defect close to the vertex where annihilation occurs is taken as the main solution and the perturbation parameter is the inverse of the distance to the opposite vertex, $1/l$. Thus,

$$q(t) = q_0(t) + \frac{1}{l} q_1(t) + \cdots, \tag{C3}$$

$$\theta(t) = \theta_0(t) + \frac{1}{l} \theta_1(t) + \cdots, \tag{C4}$$

where q_i/l^i and θ_i/l^i are the solutions of order $(1/l)^i$.

By expanding equations (C1) and (C2) in powers of the perturbation parameter we find the zeroth order equations

$$\frac{dq_0}{dt} = \zeta \frac{1}{q_0}, \tag{C5}$$

$$\frac{d\theta_0}{dt} = 0, \tag{C6}$$

whose solutions from an arbitrary time t to the annihilation time t_{anni} read as

$$q_0(t) = \sqrt{-2\zeta}\,(t_{\text{anni}} - t)^{1/2}, \tag{C7}$$

and

$$\theta_0(t) = \text{constant}. \tag{C8}$$

We also find the first order equations

$$\frac{dq_1}{dt} = -\zeta \frac{q_1}{q_0^2} - \zeta\cos\theta_0, \tag{C9}$$

and

$$\frac{d\theta_1}{dt} = -\zeta \sin\theta_0 \frac{1}{q_0}, \tag{C10}$$

whose solutions read as

$$q_1(t) = \frac{2}{3}\zeta\cos\theta_0\,(t_{\text{anni}} - t) + \frac{c_1}{\sqrt{2}}(t_{\text{anni}} - t)^{-1/2}, \tag{C11}$$

and

$$\theta_1(t) = \theta_1(t_{\text{anni}}) - \sqrt{-2\zeta}\sin\theta_0\,(t_{\text{anni}} - t)^{1/2}. \tag{C12}$$

In equation (C11), c_1 is a constant that vanishes because $q(t_{\text{anni}}) = 0$. Then, up to first order in the perturbation parameter, we obtain

$$q(t) = q_0(t) + \frac{1}{l} q_1(t) = \sqrt{-2\zeta}\,(t_{\text{anni}} - t)^{1/2} + \frac{2}{3l}\zeta\cos\theta_0\,(t_{\text{anni}} - t), \tag{C13}$$

and

$$\theta(t) = \theta_0(t) + \frac{1}{l}\theta_1(t) = \theta_{\text{anni}} - \frac{\sqrt{-2\zeta}\sin\theta_0}{l}(t_{\text{anni}} - t)^{1/2}, \tag{C14}$$

where $\theta_{\text{anni}} = \theta(t_0)$ is the angle of incidence of $\mathbf{q}$, i.e., the angle of the trajectory of the defect at the annihilation instant.

Figure S4 shows measurements of the angles $\theta_{4,+}$, $\theta_{4,-}$, and $\theta_{5,+}$ for the defects depicted in figure 14. These measurements have been fitted by equation (C14) using $\theta_{\text{anni}} = \varphi_{\text{int}}/2$ and θ_0 as adjustable parameter.

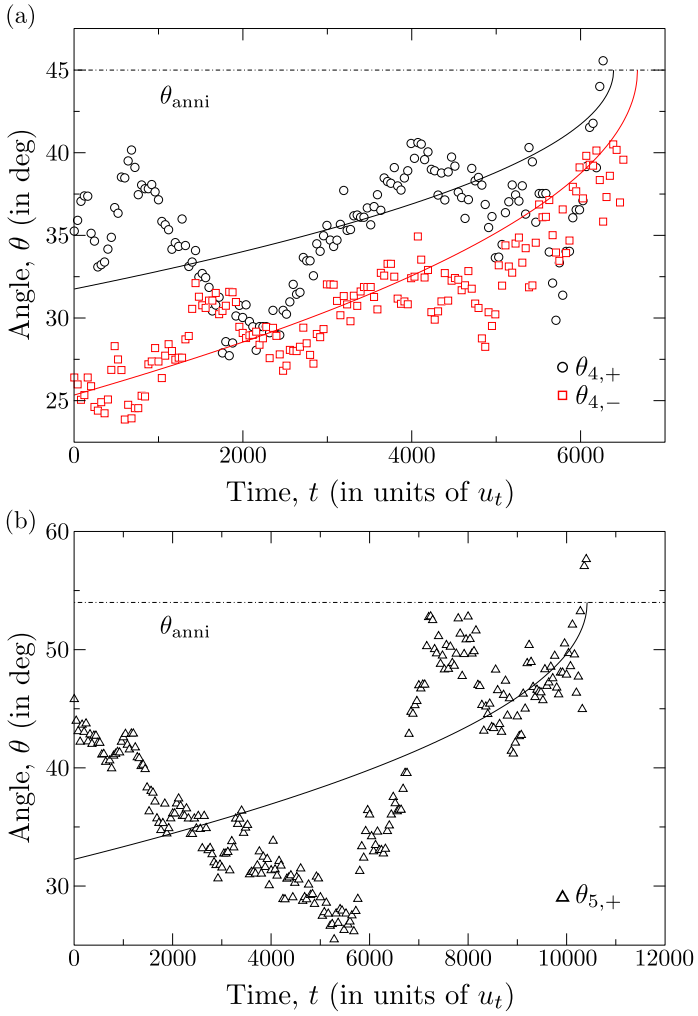

Figure S 4: Time-dependence of the angular coordinate of defects that annihilate at polygons vertices. In (a), $\theta_{4,+}$ and $\theta_{4,-}$ are the angles of defects that annihilate in a square (figure 14 (a)). In (b), $\theta_{5,+}$ is the angle of a defect annihilated within a pentagon (figure 14 (b)). Symbols correspond with simulation measurements, whereas continuous curves represent a fit based on equation (C14). The horizontal dash-dotted line indicates the assumed value of θ at the annihilation instant, θ_{anni}.

Movie captions

1. **Movie S1**: Fast relaxation of a nematic liquid crystal (NLC) system confined to a square domain, from an initial random configuration towards a *Diagonal* stable state. The corresponding changes of the elastic distortion are given by the black noisy curve in figure 7 of the main text. This animation encompasses a time interval of $4080\,u_t$, with frames separated by regular intervals of $80\,u_t$. Simulation parameters are given in section 5.1 of the main text with $U = 10$, $R = 64\,a$, $\chi_{\mathsf{HI}} = 0.1$, and $\Delta t = 1.0\,u_t$. These are the same for all the supplementary movies. Small bars represent the director field at 4000 randomly selected cells of the nematic multi-particle collision dynamics (N-MPCD) algorithm. Bars are scaled 3 times to facilitate visualization. The color bar indicates the order parameter at collision cells, S^{c}. This way of representating the director and order parameter fields is used in all the supplementary movies.

2. **Movie S2**: An alternative relaxation process for a NLC system in a square domain that converges to the *Diagonal* solution. Textures traverse the unstable state illustrated in insets $4_{\mathsf{D}}^{(\mathsf{d})}$ and $4_{\mathsf{D}}^{(\mathsf{e})}$ in figure 7 of the main text. The corresponding evolution of the elastic distortion is given by the red noisy curve in the same figure. Here, the animation ecompasses $11840\,u_t$, with frames separated by $160\,u_t$.

3. **Movie S3**: An alternative relaxation process for a NLC system in a square domain that yields the *Diagonal* solution. Textures traverse the unstable solutions illustrated in insets $4_{\mathsf{D}}^{(\mathsf{g})}$ and $4_{\mathsf{D}}^{(\mathsf{h})}$ in figure 7 of the main text. The corresponding evolution of the elastic distortion is given by the blue noisy curve in the same figure. Here, the animation ecompasses $6400\,u_t$, with frames separated by $160\,u_t$.

4. **Movie S4**: Relaxation of a NLC system confined within a square domain, from an initial random configuration towards the *Rotated* solution. Director configurations traverse the unstable solution illustrated in inset $4_{\mathsf{R}}^{(\mathsf{a})}$ in figure 8 of the main text. The corresponding evolution of the elastic distortion is given by the black noisy curve in the same figure. This movie ecompasses $1600\,u_t$, with frames uniformly separated by $40\,u_t$.

5. **Movie S5**: An alternative relaxation process for a NLC system in a square domain that yields the *Rotated* solution. Textures traverse the unstable solutions illustrated in insets $4_{\mathsf{R}}^{(\mathsf{d})}$ and $4_{\mathsf{R}}^{(\mathsf{e})}$ in figure 8 of the main text. The corresponding evolution of the elastic distortion is given by the red noisy curve in the same figure. This animation ecompasses $5120\,u_t$, with frames separated by $80\,u_t$.

6. **Movie S6**: Relaxation of an initially disordered NLC system in a pentagon domain. The confined NLC system converges to the so-called *Meta* state after exhibiting the boundary-distortion (*BD*) configuration represented in insets $5_{\mathsf{M}}^{(\mathsf{a})}$ and $5_{\mathsf{M}}^{(\mathsf{b})}$ in figure 10 of the main text. The corresponding changes of the elastic distortion are given by the black noisy curve in the same figure. This animation encompasses a time interval of $15000\,u_t$, with frames separated by regular intervals of $200\,u_t$.

7. **Movie S7**: An alternative relaxation pathway of a NLC system in a pentagon that yields the *Meta* solution. Textures traverse the unstable solutions illustrated in insets $5_{\mathsf{M}}^{(\mathsf{d})}$ and $5_{\mathsf{M}}^{(\mathsf{e})}$ in figure 10 of the main text. The corresponding changes of the elastic distortion are given by the red noisy curve in the same figure. Here, the animation ecompasses $7520\,u_t$, with frames separated by $160\,u_t$.

8. **Movie S8**: An alternative relaxation pathway of a NLC system confined to a pentagon that yields the *Meta* solution. Textures traverse the unstable solutions illustrated in insets $5_{\mathrm{M}}^{(\mathrm{g})}$ and $5_{\mathrm{M}}^{(\mathrm{h})}$ in figure 10 of the main text. The corresponding changes of the elastic distortion are given by the blue noisy curve in the same figure. Here, the animation ecompasses $10000\,u_t$, with frames separated by $160\,u_t$.

9. **Movie S9**: An alternative relaxation pathway of a NLC system confined to a pentagon that yields the *Meta* solution. Textures traverse the unstable solutions illustrated in insets $5_{\mathrm{M}}^{(\mathrm{j})}$ and $5_{\mathrm{M}}^{(\mathrm{k})}$ in figure 10 of the main text. The corresponding changes of the elastic distortion are given by the orange noisy curve in the same figure. Here, the animation ecompasses $1600\,u_t$, with frames separated by $40\,u_t$.

10. **Movie S10**: N-MPCD simulation of the relaxation process of a NLC confined within a hexagon domain. The confined fluid starts from a disordered configuration and converges to the so-called *Para* state. The corresponding evolution of the elastic distortion of the system is given by the black noisy curve in figure 12 in the main text. This animation encompasses a time interval of $16800\,u_t$, with frames separated by regular intervals of $400\,u_t$.

11. **Movie S11**: An alternative relaxation process for an initially disordered NLC system confined to a hexagon domain. The simulated NLC system converges to the *Para* state after traversing configurations $6_{\mathrm{P}}^{(\mathrm{d})}$ and $6_{\mathrm{P}}^{(\mathrm{e})}$ in figure 12 in the main text. The corresponding changes of the elastic distortion are given by the red noisy curve in the same figure. This animation encompasses $25000\,u_t$. To show the transitory states clearly, the first 10 frames are separated by $80\,u_t$; the second 8 frames are separated by $400\,u_t$; and the remaining frames are separated by $800\,u_t$.

12. **Movie S12**: An alternative relaxation process for an initially disordered NLC system confined to a hexagon domain. The simulated NLC system converges to the *Para* state after traversing configuration $6_{\mathrm{P}}^{(\mathrm{g})}$ in figure 12 in the main text. The corresponding changes of the elastic distortion are given by the blue noisy curve in the same figure. This animation encompasses $20000\,u_t$. To show the transitory states clearly, the first 14 frames are separated by $120\,u_t$ and the remaining frames are separated by $800\,u_t$.

References

[1] A. V. Zakharov, A. V. Komolkin, and A. Maliniak, *Rotational viscosity in a nematic liquid crystal: A theoretical treatment and molecular dynamics simulation*, *Phys. Rev. E*, 1999, **59**, 6802–6807.

[2] A. V. Zakharov and A. Maliniak, *Theoretical investigations of rotational phenomena and dielectric properties in a nematic liquid crystal*, *Eur. Phys. J. E*, 2001, **4**, 435–443.

[3] N. Kirov, I. Dozov and M. P. Fontana, *Determination of orientational correlation functions in ordered fluids: Raman scattering*, *J. Chem. Phys.*, 1985, **83**, 5267–5276.

[4] H. Pleiner and H. R. Brand, *Pattern Formation in Liquid Crystals*, Springer, New York, 1996, pp. 15–67.

[5] H. Híjar, R. Halver and G. Sutmann, *Spontaneous fluctuations in mesoscopic simulations of nematic liquid crystals*, *Fluct. Noise Lett.*, 2019, **18**, 1950011.

[6] H. Híjar, *Hydrodynamic correlations in isotropic fluids and liquid crystals simulated by multi-particle collision dynamics*, *Condens. Matter Phys.*, 2019, **22**, 13601.

[7] D. Reyes-Arango, J. Quintana-H, J. C. Armas-Pérez, and H. Híjar, *Defects around nanocolloids in nematic solvents simulated by Multi-particle Collision Dynamics*, *Physica A*, 2020, **547**, 123862.

[8] J. Macías-Durán, V. Duarte-Alaniz, and H. Híjar, *Active nematic liquid crystals simulated by particle-based mesoscopic methods*, *Soft Matter*, 2023, **19**, 8052–8069.

[9] D. J. Cleaver and M. P. Allen, *Computer simulations of the elastic properties of liquid crystals*, *Phys. Rev. A*, 1991, **43**, 1918–1931.

[10] T. N. Shendruk and J. M. Yeomans, *Multi-particle collision dynamics algorithm for nematic fluids*, *Soft Matter*, 2015, **11**, 5101–5110.

[11] H. Híjar, *Dynamics of defects around anisotropic particles in nematic liquid crystals under shear*, *Phys. Rev. E*, 2020, **102**, 062705.